Design of Bifunctional Nb/V Interfaces for Improving Reversible Hydrogen Storage Performance of MgH$_2$

Yang Meng, Shunlong Ju, Wei Chen, Xiaowei Chen, Guanglin Xia,* Dalin Sun, and Xuebin Yu*

While MgH$_2$ has been widely regarded as a promising solid-state hydrogen storage material, the high operating temperature and sluggish kinetics pose a major bottleneck for its practical application. Herein, V$_4$Nb$_{18}$O$_{55}$ microspheres composed of nanoparticles with size of tens of nanometers are fabricated to promote H$_2$ desorption and absorption properties of MgH$_2$, which results in the uniform formation of Nb/V interfaces based on a molecular scale during the reversible hydrogen storage process. It is experimentally and theoretically demonstrated that the uniform building of Nb/V interfaces not only preserves the ability of Nb in weakening Mg-H bonds but also alleviates the strong adsorption capacity of metallic Nb toward hydrogen atoms, leading to a relative energy barrier for the whole dehydrogenation process of MgH$_2$ of only 0.5 eV, which is 0.22 and 0.43 eV lower than that of Nb and V, respectively. As a result, under the addition of V$_4$Nb$_{18}$O$_{55}$ microspheres, the onset H$_2$ desorption temperature of MgH$_2$ is decreased to 165 °C, 125 °C lower than that of bulk MgH$_2$, and the complete hydrogenation of Mg could be realized even at room temperature, while almost no H$_2$ adsorption is observed for bulk Mg at a high temperature of 50 °C.

1. Introduction

Hydrogen is regarded as one of the best candidates for future low-carbon energy systems,[1] while its safe and efficient storage, with high gravimetric and volumetric capacity, is a major bottleneck for its practical application.[2] As one of the most investigated hydrogen storage materials, magnesium hydride (MgH$_2$) attracts extensive attention due to its high gravimetric capacity

(7.6 wt%), favorable reversibility, and abundant natural resources.[3] The operating temperature for reversible hydrogen storage of MgH$_2$, however, is over 400 °C in general due to its high thermodynamic stability and kinetic barrier.[4]

To date, considerable efforts have been devoted to improving reversible H$_2$ desorption and absorption performance of MgH$_2$ via nanosizing, catalyst doping, or the combination of them.[5] Owing to the unique 3d electronic structure, transition metal and their compounds have been widely investigated and demonstrated as effective catalysts to lower the operating temperature of MgH$_2$.[6] Among them, Nb-based compounds, especially Nb$_2$O$_5$, are representative and typical catalysts that play an efficient catalytic role in facilitating H$_2$ desorption and adsorption process of MgH$_2$.[7] Moreover, the catalytic effect of Nb$_2$O$_5$ could be further optimized by tailoring the electronic state of Nb, e.g., the introduction of Nb into Nb$_2$O$_5$ via mechanical milling, the modification of N into Nb$_2$O$_5$, and the fabrication of complex metal oxides of Nb$_2$O$_5$.[8] These oxides, however, would be reduced down to low-valence metal oxides and even zero-valence metals during the hydrogen storage process of MgH$_2$, which hence results in multi-element and/or multi-valence chemical environment.[7d,9a] It has been proposed that, due to their high electronegativity, these low-valence Nb-based species would compete with Mg as the electron donor and hence weaken Mg-H bonds, which leads to the enhanced H$_2$ desorption and adsorption process of MgH$_2$.[5b,7e] Despite these research progress, the operating temperature catalyzed by Nb-based catalysts is still over 250 °C in general and the mechanism behind the limitation of catalytic effect of Nb-based catalysts is far from clear.

Herein, to improve the catalytic role of Nb$_2$O$_5$ in improving the hydrogen storage performance of MgH$_2$, we investigate the role of slight introduction of V into Nb$_2$O$_5$ that is facile realized by building V$_4$Nb$_{18}$O$_{55}$ microspheres constructed by V$_4$Nb$_{18}$O$_{55}$ nanoparticles. This structure not only facilitates the uniform distribution of V$_4$Nb$_{18}$O$_{55}$ nanoparticles inside of MgH$_2$ matrix to facilitate its catalytic effect but also ensures the homogenous building of Nb/V interfaces based on a molecular scale. Interestingly, bulk V$_4$Nb$_{18}$O$_{55}$ nanoparticles exhibit superior catalytic effect in both Nb$_2$O$_5$ and V$_2$O$_5$, and, due to the high reductive ability of MgH$_2$ and Mg, these oxides are

Y. Meng, S. Ju, W. Chen, G. Xia, D. Sun, X. Yu
Department of Materials Science
Fudan University
Shanghai 200433, China
E-mail: xiaguanglin@fudan.edu.cn; yuxuebin@fudan.edu.cn

X. Chen
Department of Physics
Jimei University
Xiamen 361021, China

ⓘ The ORCID identification number(s) for the author(s) of this article can be found under https://doi.org/10.1002/sstr.202200119.

inevitably reduced during the reversible hydrogen storage process of MgH_2, leading to the formation of metallic V and Nb, as well as other Nb-containing species with low valence.[9] It is theoretically and experimentally demonstrated that metallic Nb-based compounds exhibit best catalytic effect than other Nb-containing compounds. The cleavage of Mg-H bonds is spontaneous under the catalysis of Nb, and the relative energy barrier for the bonding of these hydrogen atoms from the surface of Nb, however, reaches 0.88 eV due to its strong adsorption capacity toward hydrogen, which is responsible for the limited catalytic effect of Nb-based compounds. By comparison, although a high energy barrier of 0.78 eV is observed for the cleavage of Mg-H bonds under the catalysis of metallic V, the bonding of hydrogen atoms from its surface is only 0.15 eV. Impressively, the uniform building of Nb/V interfaces not only preserves the ability of Nb in weakening Mg-H bonds but also alleviates the strong adsorption capacity of metallic Nb toward hydrogen atoms, which hence leads to an energy barrier for the whole dehydrogenation process of MgH_2 of only 0.5 eV. As a result, under the catalysis of $V_4Nb_{18}O_{55}$ microspheres, the onset H_2 desorption temperature of MgH_2 is significantly decreased down to 165 °C, 125 °C lower than that of bulk MgH_2, and complete hydrogenation of Mg could be facile achieved even at room temperature. More impressively, a stable reversible capacity of 6.0 wt% could be achieved for MgH_2 for 10 cycles.

2. Results and Discussion

As schematically illustrated in **Figure 1**a, $V_4Nb_{18}O_{55}$ microspheres were synthesized by a solvothermal reaction strategy followed by thermal calcination under air. X-Ray diffraction (XRD) patterns exhibit the characteristic diffraction peaks of $V_4Nb_{18}O_{55}$ (PDF#46-0087) after the calcination of the amorphous Nb and V oxide solid solution precursor obtained from the solvothermal reaction (Figure 1b), which directly demonstrates the formation of spinel $V_4Nb_{18}O_{55}$. The valence states of V and Nb of the as-synthesized $V_4Nb_{18}O_{55}$ microspheres are further investigated by X-Ray photoelectron spectroscopy (XPS). The presence of V 2p and Nb 3d bimodal peaks at 517.3/524.5 eV and 206.6/209.6 eV could be indexed to V^{5+} and Nb^{5+},[10] respectively, which provides additional evidence to the formation of $V_4Nb_{18}O_{55}$ (Figure 1c). Moreover, the elemental analysis (Figure S1, Supporting Information) and XPS survey spectrum
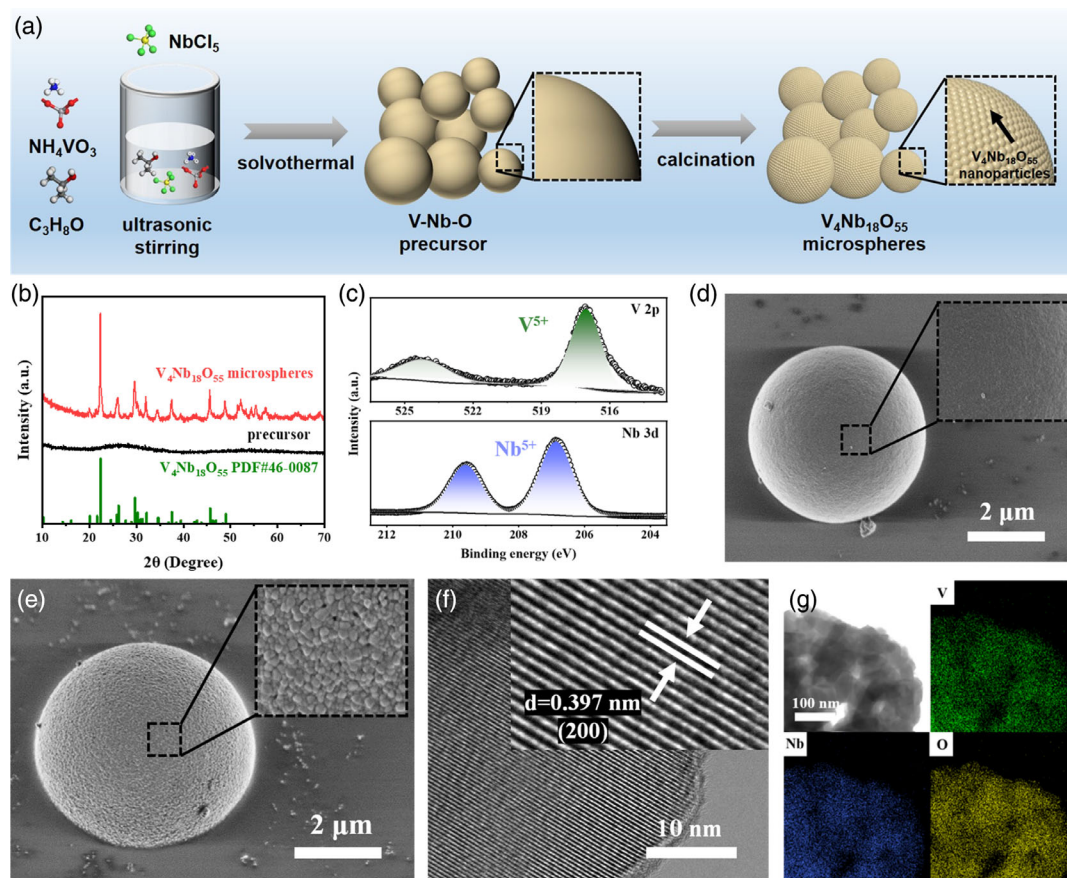

Figure 1. a) Schematic illustration of the synthesis process of $V_4Nb_{18}O_{55}$ microspheres. b) XRD patterns of the as-prepared precursor and $V_4Nb_{18}O_{55}$ microspheres. c) High-resolution V 2p and Nb 3d XPS spectra of $V_4Nb_{18}O_{55}$ microspheres (XPS raw data were processed using Advantage software for peak splitting and fitting). d) SEM images of as-synthesized precursor. e) SEM and f) HRTEM images of $V_4Nb_{18}O_{55}$ microspheres (Lattice parameters were measured using Digital Micrograph Software). g) STEM and the relative EDS elemental mapping images of V, Nb, and O of $V_4Nb_{18}O_{55}$ microspheres.

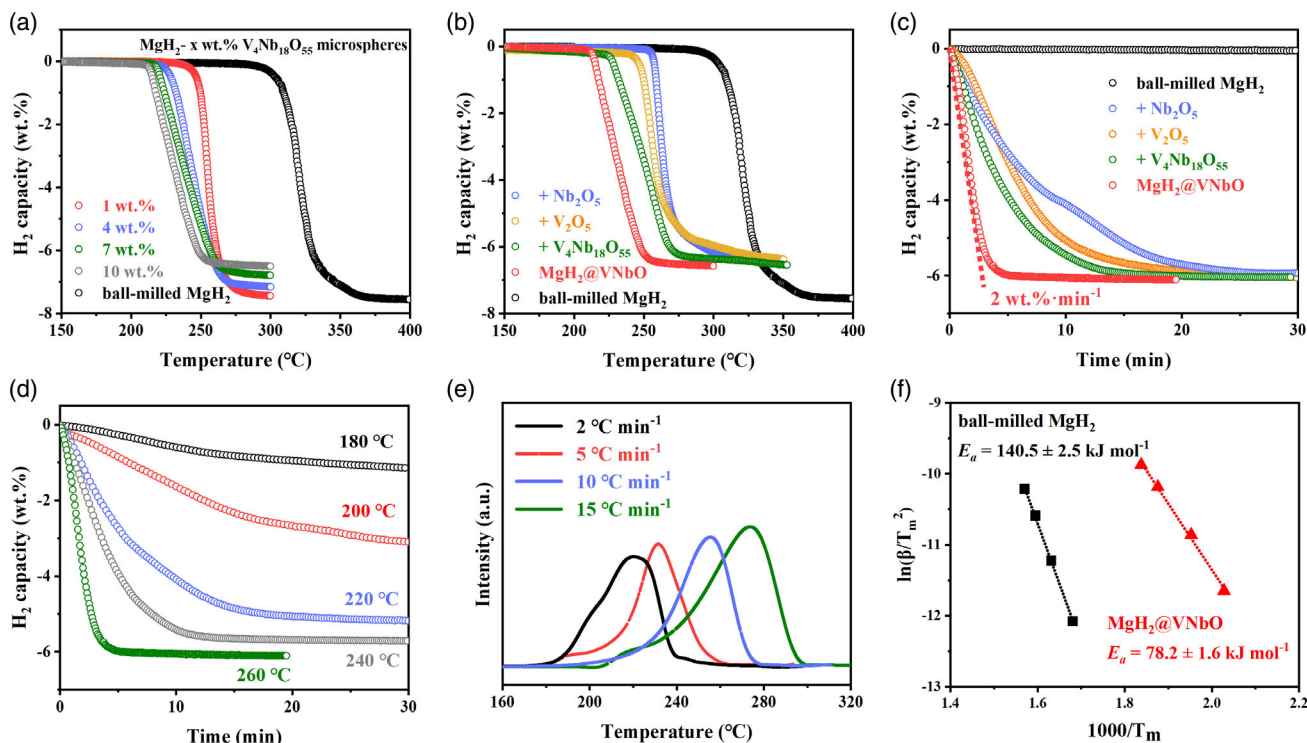**Figure 2.** a) TPD results of MgH$_2$ under the catalysis of V$_4$Nb$_{18}$O$_{55}$ microspheres with various loading ratios. b) TPD and c) isothermal H$_2$ desorption curves of MgH$_2$ at 260 °C under the catalysis of V$_4$Nb$_{18}$O$_{55}$ microspheres, with ball-milled MgH$_2$ catalyzed by bulk V$_4$Nb$_{18}$O$_{55}$, V$_2$O$_5$, and Nb$_2$O$_5$ included for comparison. d) Isothermal H$_2$ desorption curves of MgH$_2$ under the catalysis of V$_4$Nb$_{18}$O$_{55}$ microspheres. e) The differential curves of the H$_2$ desorption of MgH$_2$ under the catalysis of V$_4$Nb$_{18}$O$_{55}$ microspheres. f) Kissinger's plots of MgH$_2$ with and without the catalysis of V$_4$Nb$_{18}$O$_{55}$ microspheres (The differential curves were derived from the relative TPD curves, and data points for activation energy calculation were extracted based on the hydrogen desorption profiles presented in Figure S14 and S15, Supporting Information. With $\ln(\beta/T_m^2)$ as the y axis and $1000/T_m$ as the x axis, the Kissinger's plots were generated via linear fitting of the data points. According to the equation of the Kissinger's plots, the corresponding activation energies were then calculated using the slope values).

(Figure S2, Supporting Information) confirm that there is no chlorine residue in the as-synthesized V$_4$Nb$_{18}$O$_{55}$ microspheres. Scanning electron microscopy (SEM) images validate that the as-synthesized precursor from the solvothermal reaction are microspheres with smooth surface (**Figure 2**d and S3a, Supporting Information), which could be converted into spinel V$_4$Nb$_{18}$O$_{55}$ after the thermal treatment. Their morphology is perfectly preserved after calcination as uniform spheres but with various sizes (Figure S3b, Supporting Information). SEM and transmission electron microscopy (TEM) images demonstrate that each V$_4$Nb$_{18}$O$_{55}$ microsphere is composed of numerous primary particles with size of tens of nanometers (Figure 1e and S4, Supporting Information). High-resolution TEM (HRTEM) images exhibit the lattice fringes of 3.97 Å (inset of Figure 1f) and 3.01 Å (inset of Figure S5, Supporting Information), corresponding to the (200) and (035) planes of V$_4$Nb$_{18}$O$_{55}$, respectively, which is in good agreement with XRD and XPS results. Interestingly, scanning TEM (STEM) image illustrates the as-synthesized V$_4$Nb$_{18}$O$_{55}$ microspheres are constructed by V$_4$Nb$_{18}$O$_{55}$ nanoparticles (Figure 1g), which would promote the uniform distribution of V$_4$Nb$_{18}$O$_{55}$ microspheres with MgH$_2$ during mechanical milling process. Energy-dispersive spectroscopy (EDS) elemental mapping results demonstrate the uniform distribution of V, Nb, and O elements in the

as-synthesized V$_4$Nb$_{18}$O$_{55}$ microspheres. For comparison, bulk V$_4$Nb$_{18}$O$_{55}$, V$_2$O$_5$, and Nb$_2$O$_5$ particles are also synthesized based on the similar synthetic procedure, which have particle sizes of several microns with irregular morphology as evidenced by XRD patterns (Figure S6, Supporting Information) and SEM images (Figure S7 and S8, Supporting Information).

The catalytic effect of V$_4$Nb$_{18}$O$_{55}$ microspheres in improving hydrogen storage performance of MgH$_2$ is first evaluated by mixing V$_4$Nb$_{18}$O$_{55}$ microspheres and MgH$_2$ with various weight percent. After the milling process, XRD patterns reveal that the main characteristic diffraction peaks of MgH$_2$ catalyzed by V$_4$Nb$_{18}$O$_{55}$ microspheres could be indexed to MgH$_2$ with the appearance of weak peaks of MgO (Figure S9, Supporting Information), indicating partial oxidation of MgH$_2$ by V$_4$Nb$_{18}$O$_{55}$ microspheres. No diffraction peaks of V$_4$Nb$_{18}$O$_{55}$ microspheres, however, could be detected, which could be attributed to its in situ reduction reaction by MgH$_2$ and/or its low content. SEM and TEM images verify that MgH$_2$ mixed with V$_4$Nb$_{18}$O$_{55}$ microspheres exhibits particle sizes ranging from 100 to 500 nm, which are comparable to that of ball-milled MgH$_2$ (Figure S10 and S11, Supporting Information), without the observation of any V$_4$Nb$_{18}$O$_{55}$ microsphere, indicating the crushing of V$_4$Nb$_{18}$O$_{55}$ microspheres during milling process. It could be further supported by EDS elemental mapping results

**ADVANCED
SCIENCE NEWS**

www.advancedsciencenews.com

**small
structures**

www.small-structures.com

(Figure S12, Supporting Information), which reveal that the distribution of V and Nb of $V_4Nb_{18}O_{55}$ microspheres corresponds well with Mg of MgH_2, indicating the homogeneous distribution of $V_4Nb_{18}O_{55}$ nanoparticles evolved from $V_4Nb_{18}O_{55}$ microspheres inside of MgH_2 matrix.

The H_2 desorption performance of MgH_2 under the catalysis of $V_4Nb_{18}O_{55}$ microspheres is first investigated via temperature-programmed desorption (TPD) test. As shown in Figure 2a, the ball-milled MgH_2 starts releasing H_2 at approximately 290 °C with a high terminal temperature at 365 °C, delivering a H_2 desorption capacity of about 7.55 wt%, which agrees well with its theoretical H_2 capacity. After the addition of only 1 wt% of $V_4Nb_{18}O_{55}$ microspheres, the onset H_2 desorption temperature of MgH_2 is significantly lowered by 50 °C with the release of 7.34 wt% of H_2 before 280 °C, which directly demonstrates the catalytic role of $V_4Nb_{18}O_{55}$ microspheres in enhancing hydrogen storage performance of MgH_2. As expected, although the increase of the amount of $V_4Nb_{18}O_{55}$ microspheres leads to the decrease of both onset and terminal H_2 desorption temperature, a significant decrease of H_2 storage capacity could be observed. Particularly, MgH_2 catalyzed by $V_4Nb_{18}O_{55}$ microspheres with a weight percent of 25 wt% exhibits comparable H_2 desorption performance with that catalyzed by 10 wt% of $V_4Nb_{18}O_{55}$ microspheres but with much less H_2 capacity (Figure S13, Supporting Information). Considering the balance between H_2 storage capacity and the operating temperature, MgH_2 catalyzed by $V_4Nb_{18}O_{55}$ microspheres with a weight percent of 10 wt% (denoted as $MgH_2@VNbO$) is selected for investigation in detail, and for comparison, the amount of all the catalysts adopted in this work is also set to 10 wt%.

It is interestingly to note that, after the addition of bulk V_2O_5 and Nb_2O_5, the onset temperature for the H_2 desorption from MgH_2 could be decreased to approximately 240 and 252 °C (Figure 2b), respectively, indicating that both V_2O_5 and Nb_2O_5 could catalytically enhance H_2 desorption performance of MgH_2. By comparison, the addition of bulk $V_4Nb_{18}O_{55}$ leads to further reduction of H_2 desorption temperature of MgH_2 down to 225 °C, demonstrating the superior catalytic effect of $V_4Nb_{18}O_{55}$ composed of both V^{5+} and Nb^{5+} than both V_2O_5 and Nb_2O_5, which indicates the presence of the synergistic effect between both V^{5+} and Nb^{5+} in improving the H_2 desorption from MgH_2. Impressively, the addition of $V_4Nb_{18}O_{55}$ microspheres results in the decrease of the onset and terminal dehydrogenation temperature of MgH_2 down to only 207 and 255 °C, which are 18 and 20 °C lower than those of bulk $V_4Nb_{18}O_{55}$, respectively. This result indicates that the decrease of particle size effectively facilitates the uniform distribution between $V_4Nb_{18}O_{55}$ microspheres and MgH_2 during ball milling process, which could be verified by the elemental mapping results that validate the homogeneous distribution of $V_4Nb_{18}O_{55}$ microspheres inside of MgH_2 matrix. It hence promotes the catalytic effect of $V_4Nb_{18}O_{55}$ in improving H_2 desorption performance of MgH_2.

Isothermal H_2 desorption kinetics of MgH_2 under the catalysis of $V_4Nb_{18}O_{55}$ microspheres are subsequently investigated. It should be noted that the subsequent H_2 desorption of MgH_2 catalyzed by these catalysts are conducted after the hydrogenation of first cycle. As shown in Figure 2c, no detectable H_2 desorption could be observed for ball-milled MgH_2 at 260 °C, while a

complete dehydrogenation of MgH_2 could be realized within approximately 20 and 30 min under the catalysis of either V_2O_5 or Nb_2O_5, respectively, indicating their catalytic role in promoting H_2 desorption performance of MgH_2. By comparison, the time required for the complete dehydrogenation of MgH_2 could be decreased to 15 min when using bulk $V_4Nb_{18}O_{55}$ as the catalyst, which provides further evidence to the superior catalytic effect of $V_4Nb_{18}O_{55}$ than both V_2O_5 and Nb_2O_5. Interestingly, under the catalysis of $V_4Nb_{18}O_{55}$ microspheres, only 5 min is required for the complete dehydrogenation of MgH_2, delivering a H_2 desorption capacity of 6.0 wt%. According to the slope of the tangent line of the curve, the H_2 desorption rate of MgH_2 catalyzed by $V_4Nb_{18}O_{55}$ microspheres is calculated to be 2 wt% min^{-1}, which is much faster than that of MgH_2 with the addition of bulk $V_4Nb_{18}O_{55}$. At the temperature of 240 °C, 5.57 wt% H_2 could be released from MgH_2 under the catalysis of $V_4Nb_{18}O_{55}$ microspheres within 10 min. Furthermore, upon decreasing the heating temperature down to 220 °C, MgH_2 catalyzed by $V_4Nb_{18}O_{55}$ microspheres is still capable of releasing 4.82 wt% H_2 within 15 min. More impressively, even at the temperature of 200 and 180 °C, about 3.15 and 1.16 wt% H_2 could be desorbed from MgH_2 under the catalysis of $V_4Nb_{18}O_{55}$ microspheres within 30 min, respectively. In order to quantitively investigate the catalytic role of $V_4Nb_{18}O_{55}$ microspheres in improving H_2 desorption kinetics of MgH_2, the apparent activation energy (E_a) is calculated based on Kissinger's method[11] according to Equation (1)

$$\frac{d(\ln\beta/T_m^2)}{d(1/T_m)} = \frac{-E_a}{R} \tag{1}$$

where β is the heating rate, T_m is the temperature that corresponds to the maximum rate of dehydrogenation, E_a is the apparent activation energy, and R is the gas constant. The value of E_a could be obtained from the slope of the plot by the Equation (1). Herein, the TPD derivative curves are used to evaluate the T_m at different heating rates (Figure 2e, S14–S16, Supporting Information). After linear fitting, the E_a of MgH_2 catalyzed by $V_4Nb_{18}O_{55}$ microspheres is determined to be approximately 78.2 kJ mol^{-1} (Figure 2f), 44.3% lower than that of ball-milled MgH_2 (i.e., 140.5 kJ mol^{-1}), which provides additional evidence to the significant improvement of H_2 desorption kinetics for MgH_2 under the catalysis of $V_4Nb_{18}O_{55}$ microspheres.

During the reversible hydrogenation process under the hydrogen pressure of 30 atm at a temperature as low as 50 °C, no detectable H_2 absorption could be observed for the dehydrogenated products of ball-milled MgH_2 within 30 min (**Figure 3**a), while a capacity of 3.59 and 2.71 wt% of H_2 could be absorbed into MgH_2 under the catalysis of bulk V_2O_5 and Nb_2O_5, respectively, indicating their catalytic role in promoting H_2 absorption performance of MgH_2. By comparison, a capacity of 4.06 wt% could be absorbed by MgH_2 under the catalysis of bulk $V_4Nb_{18}O_{55}$, which demonstrates the superior catalytic effect of $V_4Nb_{18}O_{55}$ in enhancing H_2 adsorption performance of MgH_2 than either V_2O_5 or Nb_2O_5. This result directly confirms that the synergistic catalytic effect of V and Nb simultaneously promotes H_2 absorption and desorption performance of MgH_2. More importantly, under the catalysis of $V_4Nb_{18}O_{55}$
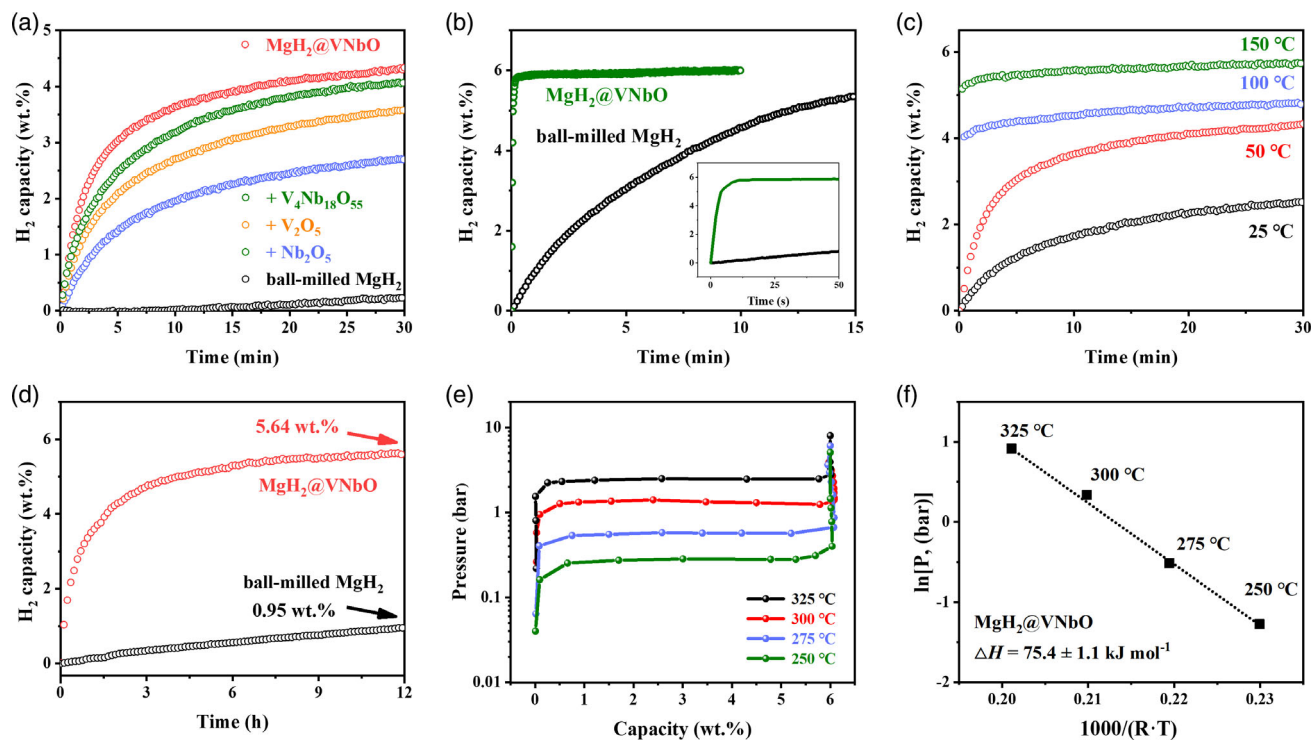
Figure 3. a) Isothermal H_2 absorption curves of MgH_2 under the catalysis of $V_4Nb_{18}O_{55}$ microspheres at 50 °C, with ball-milled MgH_2 catalyzed by bulk $V_4Nb_{18}O_{55}$, V_2O_5, and Nb_2O_5 included for comparison. b) Isothermal H_2 absorption curves of ball-milled MgH_2 and MgH_2 catalyzed by $V_4Nb_{18}O_{55}$ microspheres at 200 °C. c) Isothermal H_2 curves of MgH_2 catalyzed by $V_4Nb_{18}O_{55}$ microspheres. d) Isothermal H_2 curves of MgH_2 catalyzed by $V_4Nb_{18}O_{55}$ microspheres at room temperature, with ball-milled MgH_2 included for comparison. e) PCI curves and f) van't Hoff plot of MgH_2 under the catalysis of $V_4Nb_{18}O_{55}$ microspheres (Data points for the thermodynamic enthalpy calculation were extracted based on the PCI curves profiles presented in 3e. With $\ln(p)$ as the y axis and $1000/(R·T)$ as the x axis, the van't Hoff plots were generated via linear fitting of the data points. According to the equation of the van't Hoff plots, the corresponding thermodynamic enthalpy were then calculated using the slope values).

microspheres, the reversible capacity of MgH_2 approaches 4.34 wt% H_2 under identical condition, which further verifies that uniform distribution of $V_4Nb_{18}O_{55}$ microspheres not only improves the H_2 desorption performance MgH_2 but also greatly enhances its H_2 absorption performance. Impressively, 5.92 wt% of H_2 is recharged into the dehydrogenated MgH_2 catalyzed by $V_4Nb_{18}O_{55}$ microspheres within 20 s at 200 °C, while only a neglectable capacity of 0.35 wt% could be adsorbed into dehydrogenated bulk MgH_2 under identical conditions (Figure 3b). Upon decreasing the operating temperature down to 150 and 100 °C, 5.28 and 4.15 wt% of H_2 could be recharged into the dehydrogenated MgH_2 under the catalysis of $V_4Nb_{18}O_{55}$ microspheres within a time period of only 1 min (Figure 3c). Even at room temperature under a H_2 pressure of 50 atm, a reversible capacity of 3.35 wt% H_2 could also be achieved for MgH_2 under the catalysis of $V_4Nb_{18}O_{55}$ microspheres within an hour, and this value approaches 5.64 wt% H_2 upon extending hydrogenation time to 12 h (Figure 3d), corresponding to 94% of the theoretical reversible hydrogen capacity of this system, while ball-milled MgH_2 after complete dehydrogenation could only absorb 0.95 wt% H_2 under identical condition.

Pressure–composition isotherms (PCI) curves validate that the equilibrium pressure of H_2 desorption from MgH_2 at 250, 275, 300, and 325 °C is determined to be approximately 0.3, 0.6, 1.4, and 2.5 atm, respectively (Figure 3e). As a result, the

thermodynamic enthalpy (ΔH) of MgH_2 under the catalysis of $V_4Nb_{18}O_{55}$ microspheres calculated by the van't Hoff equation[12] is determined to be 75.4 ± 1.1 kJ mol^{-1} (Figure 3f), which is comparable to the ΔH of ball-milled MgH_2 (Figure S17, Supporting Information). It demonstrates that the introduction of $V_4Nb_{18}O_{55}$ microspheres has no effect in tuning thermodynamic stability of MgH_2, and hence the improvement of hydrogen storage performance of MgH_2 under the catalysis of $V_4Nb_{18}O_{55}$ microspheres could be attributed to its catalytic effect in promoting H_2 absorption and desorption kinetics of MgH_2.

The cycling performance demonstrates that a reversible capacity of 6.0 wt%, corresponding to a capacity retention of 97% after the second cycle, could be obtained for MgH_2 under the catalysis of $V_4Nb_{18}O_{55}$ microspheres after 10 cycles of hydrogen storage process (**Figure 4**a). More interestingly, a continuous decline of the onset temperature from 207 °C to 165 °C could be clearly observed for MgH_2 under the catalysis of $V_4Nb_{18}O_{55}$ microspheres since the second cycle of H_2 desorption process (Figure 4b), indicating the enhancement of catalytic effect of $V_4Nb_{18}O_{55}$ microspheres upon cycling process. Since the second cycle, MgH_2 could liberate approximately 97% of its theoretical H_2 capacity before 240 °C under the catalysis of $V_4Nb_{18}O_{55}$ microspheres, and the peak temperature for H_2 desorption is significantly decreased to 220 °C (Figure S18, Supporting Information), which is among the best reported MgH_2-based
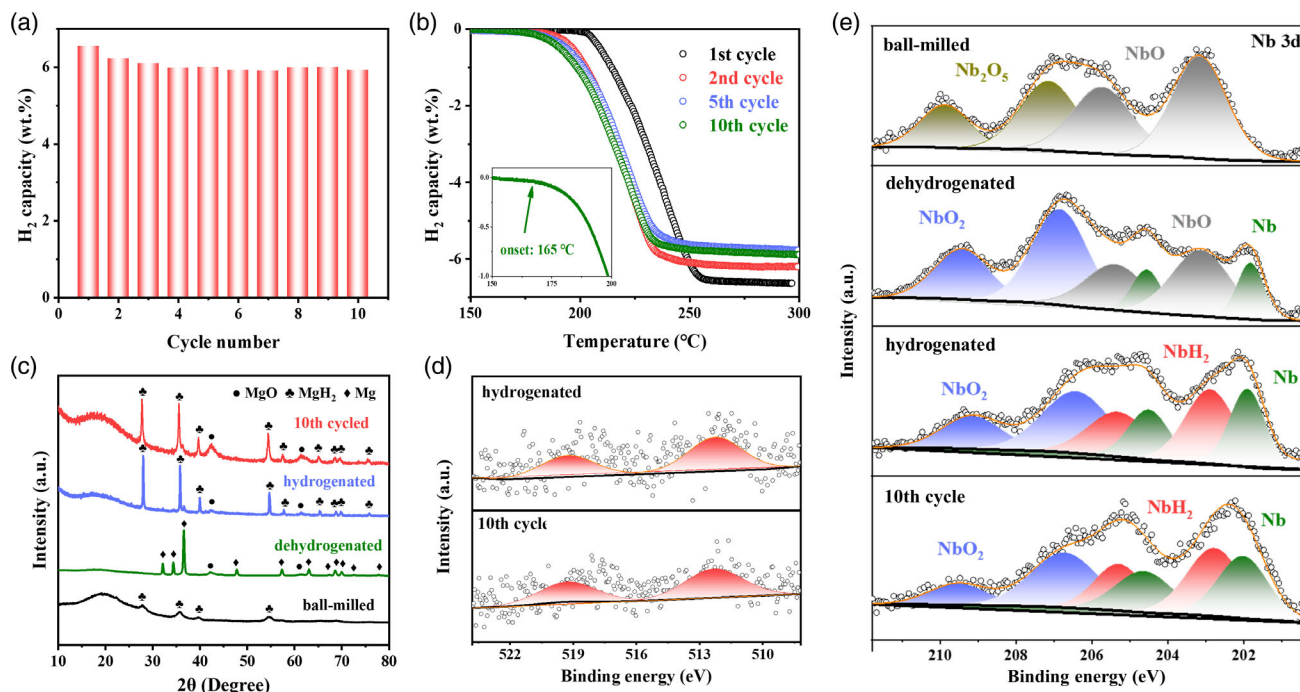
Figure 4. a) The reversible capacity and b) TPD results of MgH_2 catalyzed by $V_4Nb_{18}O_{55}$ microspheres upon cycling. c) XRD patterns, and high-resolution d) V 2p and e) Nb 3d XPS spectra of MgH_2 under the catalysis of $V_4Nb_{18}O_{55}$ microspheres at various states (XPS raw data were processed using Advantage software for peak splitting and fitting).

hydrogen storage materials so far (Table S1, Supporting Information). By comparison, although the H_2 desorption performance of MgH_2 under the catalysis of V_2O_5 or Nb_2O_5 could also be improved to some extent, the onset temperature for H_2 desorption of MgH_2 under the catalysis of V_2O_5 or Nb_2O_5 is still much higher than that of MgH_2 under the catalysis of $V_4Nb_{18}O_{55}$ under identical condition (Figure S19, Supporting Information). This result provides additional evidence for the presence of the synergistic effect between V and Nb in improving hydrogen storage performance of MgH_2. EDS elemental mapping results (Figure S20, Supporting Information) reveal that the uniform distribution of V and Nb in MgH_2 matrix could be well preserved after 10 cycles, which contributes to stable reversibility of MgH_2.

In order to understand the improved catalytic effect of $V_4Nb_{18}O_{55}$ microspheres upon repeated H_2 adsorption and desorption process, the chemical states of MgH_2 at different stages are characterized in detail. XRD results demonstrate the reversible transformation between Mg and MgH_2 during H_2 desorption and adsorption process (Figure 4c). After 10 cycles, the main characteristic diffraction peaks of MgH_2 under the catalysis of $V_4Nb_{18}O_{55}$ microspheres could also be indexed to MgH_2, which provides additional evidence for the stable reversibility of MgH_2. No diffraction peaks belonging to $V_4Nb_{18}O_{55}$ microspheres, however, could be identified, which possibly could be attributed to the in situ reduction of $V_4Nb_{18}O_{55}$ microspheres and/or its low content. Hence, XPS analysis and HRTEM measurement are further conducted to analyze the changes of V and Nb of $V_4Nb_{18}O_{55}$ microspheres. It should be mentioned that the proportion of catalysts is increased to 25 wt% to ensure the valid identification of the states of V and Nb during the

characterization of XPS and HRTEM measurement. The first and second H_2 desorption curves of MgH_2 with a weight percent of 25 wt% $V_4Nb_{18}O_{55}$ microspheres exhibit comparable with that with the addition of 10 wt% of $V_4Nb_{18}O_{55}$ microspheres (Figure S13, Supporting Information), indicating that the phase evolution of V and Nb of $V_4Nb_{18}O_{55}$ microspheres is consistent. The difference of their onset temperature could be induced by the formation of smaller MgH_2 particles due to the increased content of the oxides as grinding assistants during ball milling.[13]

Despite the increased content of $V_4Nb_{18}O_{55}$ microspheres, the signals of V in MgH_2 catalyzed by $V_4Nb_{18}O_{55}$ microspheres after ball milling and dehydrogenation could not be accurately identified (Figure S21, Supporting Information). After the subsequent hydrogenation process, the spin-orbit double peaks at 512.6 and 519.8 eV in the V 2p XPS spectra (Figure 4d) could be indexed to V^0,[9b] indicating that V^{5+} of $V_4Nb_{18}O_{55}$ microspheres is reduced to V^0. Moreover, the signal of V^0 is well preserved after 10 cycles of H_2 adsorption process, demonstrating the stable formation of metallic V. By comparison, the valence of Nb could be clearly detected by XPS spectra of MgH_2 catalyzed by $V_4Nb_{18}O_{55}$ microspheres (Figure 4e). The ball milling process leads to only partial reduction of Nb^{5+}, with the observation of NbO at 202.8 and 205.6 eV in the Nb 3d XPS spectra.[7e,9a] After the initial dehydrogenation process, the valence state of Nb is further reduced with the complete disappearance of Nb^{5+},[7c,7d] accompanied by the formation of Nb, NbO, and NbO_2, indicating that Nb^{5+} of $V_4Nb_{18}O_{55}$ microspheres is in situ transformed to Nb, NbO, and NbO_2. The subsequent hydrogenation process results in the detection of new peaks at 203.4 and 206.0 eV that could

be indexed to NbH_2.[7c,14] Hence, it could be concluded that $V_4Nb_{18}O_{55}$ microspheres are in situ transformed into metallic V and Nb, NbH_2, NbO, and NbO_2, which could be regarded as the actual catalysts that facilitate the H_2 desorption and adsorption process of MgH_2.

Subsequently, TEM and HRTEM are used to clarify the evolution of microstructure of MgH_2 under the catalysis of $V_4Nb_{18}O_{55}$ microspheres (**Figure 5**, S22 and S23, Supporting Information). The well-distributed dark regions in these images could be identified as the nanoparticles from the broken $V_4Nb_{18}O_{55}$ microspheres during ball milling process, which further demonstrates the uniform distribution of $V_4Nb_{18}O_{55}$ nanoparticles inside of MgH_2 matrix (Figure 5a–c). HRTEM images illustrate the obvious lattice spacings of 0.245 and 0.251 nm that could be indexed to the (101) planes of Mg and the (101) planes of MgH_2, respectively, indicating the reversible transformation between Mg and MgH_2 during H_2 desorption and adsorption process, which agrees well with the XRD results. After the initial hydrogenation process, the lattice spacing of 0.214 nm that could be indexed to the (110) plane of metallic V is observed in the HRTEM image, corresponding well with the XPS results. In addition, after the dehydrogenation process, HRTEM images exhibit obviously lattice spacings of 0.233, 0.148, and 0.255 nm that could be indexed to the (110) planes of metallic Nb, the (022) planes of NbO, and the (222) planes of NbO_2, respectively, which also agrees well with the XPS results. After the hydrogenation process, the new lattice spacings of 0.228 and 0.263 nm could be observed, which are indexed to the (200) and (111) planes of NbH_2, respectively. Owing to the in situ reduction of $V_4Nb_{18}O_{55}$ based on a molecular scale, the

homogeneous distribution of numerous Nb/V interfaces that are uniformly distributed inside of MgH_2 could be clearly observed during the reversible hydrogen storage process (Figure 5e,f). As a result, it could be concluded that the difference between the first and second dehydrogenation process of MgH_2 under the catalysis of $V_4Nb_{18}O_{55}$ microspheres could be attributed to the transformation of active catalysts. Moreover, the thus-formed metallic V and Nb, NbH_2, and NbO_2 from the in situ transformation of $V_4Nb_{18}O_{55}$ microspheres are well preserved after 10 cycles of H_2 desorption and adsorption process, which contributes to the stable cycling hydrogen storage performance of MgH_2.

In order to reveal the catalytic role of Nb and V species in the H_2 desorption of MgH_2, theoretical calculation is conducted based on density functional theory (DFT). It is calculated that the length of Mg-H bonds in the pristine MgH_2 monomer is 1.71 Å, and only limited change of the length of Mg-H bonds could be observed for MgH_2 under the catalysis of Nb_2O_5 and V_2O_5 (Figure S24, Supporting Information). Interestingly, under the catalysis of metallic V, metallic Nb, NbO, NbH_2, and NbO_2, the corresponding Mg-H bonds are largely stretched to 2.06, 2.58, 1.76, 1.85, and 2.28 Å, respectively (Figure S24 and S25, Supporting Information). This result indicates that the in situ formed V and Nb species upon the hydrogenation and dehydrogenation as verified by XPS and HRTEM results could effectively weaken Mg-H bonds, which is capable of promoting hydrogen storage performance of MgH_2. This phenomenon could be attributed to the electron transfer to MgH_2 from the surface of V and Nb species due to their larger electronegativity, resulting in the weakening of Mg-H bonds (Figure S25, Supporting
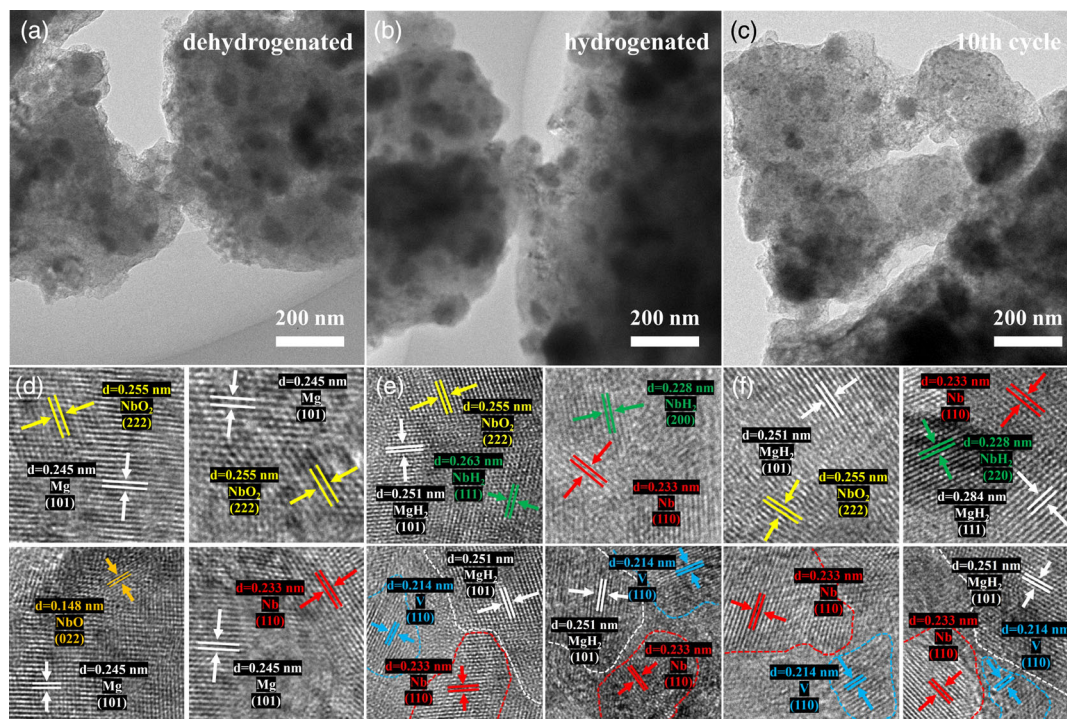

Figure 5. a–c) TEM and d–f) the relative HRTEM images of MgH_2 under the catalysis of $V_4Nb_{18}O_{55}$ microspheres at various states (Lattice parameters were measured using Digital Micrograph Software).

Information). Among them, the catalytic effect of metallic Nb is most effective, and obvious adsorption of H from MgH_2 could be even observed by the surface of Nb after only structural modification owing to a large charge transfer of 0.58|e| from metallic Nb to MgH_2.

To quantitatively understand the synergistic catalytic effect of these V and Nb species, the energy barrier for the dehydrogenation process of MgH_2 on V (100) and Nb (110) are subsequently calculated, as schematically illustrated in **Figure 6**. The detailed H_2 desorption process from MgH_2 is hypothesized as a two-step reaction. MgH_2 adsorbed on different substrates (initial state, denoted as IS) undergoes the breakage of Mg-H bonds to the transition state (TS), followed by the escape of H atoms from the substrate and their aggregation into H_2 (final state, denoted as FS). As shown in Figure S26, Supporting Information, the relative energy barrier for H_2 desorption from pristine MgH_2 is calculated to be 1.72 eV, indicating the presence of large kinetic barrier for its H_2 desorption, which corresponds well with its high operating temperature for dehydrogenation. In strong

contrast, under the catalysis of metallic V and Nb, the energy barrier is significantly decreased to 0.93 and 0.72 eV, respectively, which directly demonstrates their superior catalytic effect in reducing the operating temperature for H_2 desorption (Figure 6d). Specifically, the energy barrier of the decomposition of MgH_2 and the bonding of hydrogen atoms on V (110) is calculated to be 0.78 and 0.15 eV, respectively, indicating that metallic V exhibits superior catalytic effect in facilitating the bonding of hydrogen atom but has limited effect in promoting the cleavage of Mg-H bonds, which could be explained by the low charge transfer of 0.40|e| from metallic V to MgH_2 (Figure S25, Supporting Information). By comparison, the decomposition of MgH_2 on metallic Nb is spontaneous, which could be induced by the effective effect of Nb in breaking Mg-H bonds and adsorbing hydrogen atoms owing to the large charge transfer of 0.58|e| from metallic Nb to MgH_2. The energy barrier of the bonding of hydrogen atoms, however, is calculated to be as high as 0.88 eV, much higher than that under the catalysis of metallic V. This result indicates that, although metallic Nb leads to the spontaneous breakage of Mg-H bonds, its strong adsorption capacity of hydrogen atoms hinders the subsequent bonding of these hydrogen atoms. Hence, the relative energy for the whole dehydrogenation process of MgH_2 under the catalysis of metallic Nb is comparable to that of metallic V.

Interestingly, after coupling the interface of metallic Nb and V, a much lower relative energy barrier could be observed for both the breakage of Mg-H bonds in comparison to metallic V and the bonding of hydrogen atoms in comparison to metallic V and Nb. This result indicates that the synergistic effect of Nb/V interfaces could not only preserve the ability of Nb in weakening Mg-H bonds but also alleviate the strong adsorption capacity of metallic Nb toward hydrogen atoms, which could hence effectively promote the bonding of these hydrogen atoms. It could be directly supported by the integrated charge donation from both metallic Nb and V at their interfaces. As a result, under the catalysis of Nb/V interfaces, the relative energy required for the whole dehydrogenation process of MgH_2 is calculated to be 0.5 eV (Figure 6d), which is much lower than that of either metallic Nb or V. This result confirms the synergistic catalytic effect of Nb/V composite in decreasing H_2 desorption temperature of MgH_2, which correlates well with the lower H_2 desorption temperature of MgH_2 under the catalysis of $V_4Nb_{18}O_{55}$ than V_2O_5 or Nb_2O_5 (Figure 2 and S14, Supporting Information). In addition, during the H_2 desorption and adsorption of MgH_2, the in situ formation of these nanostructured actual catalytic species could ensure their uniform distribution inside of MgH_2 matrix as verified by TEM images (Figure S20, Supporting Information), which could effectively promote their catalytic effect in improving the reversible hydrogen storage performance of MgH_2 that is advanced compared to some other reported works under the same condition (Figure S27, Supporting Information).
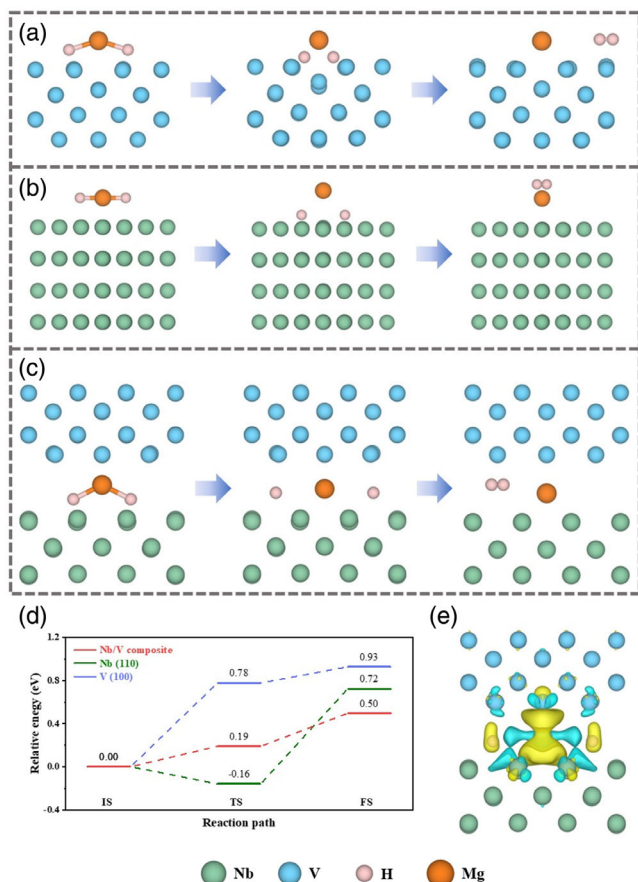

Figure 6. a–c) Schematic illustration of the H_2 desorption process of MgH_2 on V (100), Nb (110), and Nb/V composites, respectively. d) Calculated energy profiles for the H_2 desorption of MgH_2 on V (100), Nb (110), and Nb/V composites, respectively. e) Charge density difference plot for the transition state of the dehydrogenation of MgH_2 on Nb/V composites. Areas of charge accumulation are shown in yellow, while charge depletion are shown in blue.

3. Conclusion

In this work, $V_4Nb_{18}O_{55}$ microspheres composed of nanoparticles are fabricated to promote the catalytic effect of Nb_2O_5 in improving the reversible hydrogen storage properties of MgH_2, which not only results in the uniform distribution of

ADVANCED
SCIENCE NEWS
www.advancedsciencenews.com

small
structures
www.small-structures.com

$V_4Nb_{18}O_{55}$ inside of MgH_2 matrix to effectively improve its catalytic effect but also ensures the homogenous building of Nb/V interfaces based on a molecular scale during the H_2 desorption and adsorption process. It is experimentally and theoretically demonstrated that the uniform building of Nb/V interfaces not only preserves the effective ability of Nb in weakening Mg-H bonds but also alleviates the strong adsorption capacity of metallic Nb toward hydrogen atoms, hence leading to a relative energy barrier for the whole dehydrogenation process of MgH_2 of only 0.5 eV, which is 0.22 and 0.43 eV lower than that of metallic Nb and V, respectively. As a result, under the catalysis of $V_4Nb_{18}O_{55}$ microspheres, the onset and peak H_2 desorption temperatures of MgH_2 are reduced down to 165 and 220 °C, 125 and 105 °C lower than that of pristine MgH_2, respectively. Moreover, complete hydrogenation of Mg under the catalysis of $V_4Nb_{18}O_{55}$ microspheres could be achieved even at room temperature upon the reversible H_2 adsorption process, while almost no H_2 adsorption is observed for bulk Mg at a high temperature of 50 °C. More impressively, a stable reversible capacity of 6.0 wt% could be realized for MgH_2 for 10 cycles. This study provides a promising approach to modify the catalytic effect of various metal-based catalysts toward enhanced hydrogen storage performance of metal hydrides.

Supporting Information

Supporting Information is available from the Wiley Online Library or from the author.

Conflict of Interest

The authors declare no conflict of interest.

Data Availability Statement

The data that support the findings of this study are available in the supplementary material of this article.

[1] L. Schlapbach, A. Zuttel, *Nature* **2001**, *414*, 353.

[2] a) J. Yang, A. Sudik, C. Wolverton, D. J. Siegel, *Chem. Soc. Rev.* **2010**, *39*, 656; b) M. Yadav, T. Akita, N. Tsumori, Q. Xu, *J. Mater. Chem.* **2012**, *22*, 12582; c) M. B. Ley, L. H. Jepsen, Y. S. Lee, Y. W. Cho, J. M. B. von Colbe, M. Dornheim, M. Rokni, J. O. Jensen, M. Sloth, Y. Filinchuk, J. E. Jorgensen, F. Besenbacher, T. R. Jensen, *Mater. Today* **2014**, *17*, 122; d) Y. Jia, C. H. Sun, S. H. Shen, J. Zou, S. S. Mao, X. D. Yao, *Renewable Sustainable Energy Rev.* **2015**, *44*, 289; e) R. Mohtadi, S. I. Orimo, *Nat. Rev. Mater.* **2017**, *2*, 1; f) L. Z. Ouyang, W. Chen, J. W. Liu, M. Felderhoff, H. Wang, M. Zhu, *Adv. Energy Mater.* **2017**, *7*, 170029; g) Y. Y. Zhu, L. Z. Ouyang, H. Zhong, J. W. Liu, H. Wang, H. Y. Shao, Z. G. Huang, M. Zhu, *Angew. Chem., Int. Ed.* **2020**, *59*, 8623.

[3] X. Yu, Z. Tang, D. Sun, L. Ouyang, M. Zhu, *Prog. Mater. Sci.* **2017**, *88*, 1.

[4] a) K. F. Aguey-Zinsou, J. R. Ares-Fernandez, *Energy Environ. Sci.* **2010**, *3*, 526; b) T. Sadhasivam, H. T. Kim, S. Jung, S. H. Roh, J. H. Park, H. Y. Jung, *Renewable Sustainable Energy Rev.* **2017**, *72*, 523; c) Y. H. Sun, C. Q. Shen, Q. W. Lai, W. Liu, D. W. Wang, K. F. Aguey-Zinsou, *Energy Storage Mater.* **2018**, *10*, 168; d) J. G. Zhang, Y. F. Zhu, L. L. Yao, C. Xu, Y. N. Liu, L. Q. Li, *J. Alloys Compd.* **2019**, *782*, 796.

[5] a) X. Zhang, Y. Liu, Z. Ren, X. Zhang, J. Hu, Z. Huang, Y. Lu, M. Gao, H. Pan, *Energy Environ. Sci.* **2021**, *14*, 2302; b) K. Wang, X. Zhang, Y. Liu, Z. Ren, X. Zhang, J. Hu, M. Gao, H. Pan, Y. Liu, *Chem. Eng. J.* **2021**, *406*, 126831; c) T. Huang, X. Huang, C. Hu, J. Wang, H. Liu, H. Xu, F. Sun, Z. Ma, J. Zou, W. Ding, *Chem. Eng. J.* **2021**, *421*, 127851; d) H. Liu, C. Lu, X. Wang, L. Xu, X. Huang, X. Wang, H. Ning, Z. Lan, J. Guo, *ACS Appl. Mater. Interfaces* **2021**, *13*, 13235; e) X. Lu, L. Zhang, H. Yu, Z. Lu, J. He, J. Zheng, F. Wu, L. Chen, *Chem. Eng. J.* **2021**, *422*, 130101; f) Z. Ma, S. Panda, Q. Zhang, F. Sun, D. Khan, W. Ding, J. Zou, *Chem. Eng. J.* **2021**, *406*, 126790; g) G. Xia, Y. Tan, X. Chen, D. Sun, Z. Guo, H. Liu, L. Ouyang, M. Zhu, X. Yu, *Adv. Mater.* **2015**, *27*, 5981; h) Y. Huang, G. Xia, J. Chen, B. Zhang, Q. Li, X. Yu, *Prog. Nat. Sci.: Mater. Int.* **2017**, *27*, 81; i) X. Zhang, Z. Leng, M. Gao, J. Hu, F. Du, J. Yao, H. Pan, Y. Liu, *J. Power Sources* **2018**, *398*, 183; j) W. Zhu, S. Panda, C. Lu, Z. Ma, D. Khan, J. Dong, F. Sun, H. Xu, Q. Zhang, J. Zou, *ACS Appl. Mater. Interfaces* **2020**, *12*, 50333.

[6] a) L. Zhang, Z. Sun, Z. Cai, N. Yan, X. Lu, X. Zhu, L. Chen, *Appl. Surf. Sci.* **2020**, *504*, 144465; b) M. Zhang, X. Xiao, B. Luo, M. Liu, M. Chen, L. Chen, *J. Energy Chem.* **2020**, *46*, 191; c) J. Cui, H. Wang, J. W. Liu, L. Z. Ouyang, Q. A. Zhang, D. L. Sun, X. D. Yao, M. Zhu, *J. Mater. Chem. A* **2013**, *1*, 5603.

[7] a) T. Ma, S. Isobe, Y. M. Wang, N. Hashimoto, S. Ohnuki, *J. Phys. Chem. C* **2013**, *117*, 10302; b) M. S. Yahya, M. Ismail, *J. Phys. Chem. C* **2018**, *122*, 11222; c) Y. N. Liu, H. G. Gao, Y. F. Zhu, S. Y. Li, J. G. Zhang, L. Q. Li, *Appl. Surf. Sci.* **2019**, *493*, 431; d) Z. Wang, X. Zhang, Z. Ren, Y. Liu, J. Hu, H. Li, M. Gao, H. Pan, Y. Liu, *J. Mater. Chem. A* **2019**, *7*, 14244; e) L. Zhang, K. Wang, Y. Liu, X. Zhang, J. Hu, M. Gao, H. Pan, *Nano Res.* **2020**, *14*, 148; f) A. R. Yavari, J. F. R. de Castro, G. Vaughan, G. Heunen, *J. Alloys Compd.* **2003**, *353*, 246.

[8] a) Z. Q. Lan, H. Fu, R. L. Zhao, H. Z. Liu, W. Z. Zhou, H. Ning, J. Guo, *Chem. Eng. J.* **2022**, *431*, 133985; b) K. Wang, X. Zhang, Z. Ren, X. Zhang, J. Hu, M. Gao, H. Pan, Y. Liu, *Energy Storage Mater.* **2019**, *23*, 79; c) K. C. Xian, M. H. Wu, M. X. Gao, S. Wang, Z. L. Li, P. Y. Gao, Z. H. Yao, Y. F. Liu, W. P. Sun, H. G. Pan, *Small* **2022**, *595*, 2107013.

[9] a) X. L. Zhang, K. Wang, X. Zhang, J. J. Hu, M. X. Gao, H. G. Pan, Y. F. Liu, *Int. J. Energy Res.* **2021**, *45*, 3129; b) Z. Y. Wang, Z. H. Ren,

N. Jian, M. X. Gao, J. J. Hu, F. Du, H. G. Pan, Y. F. Liu, *J. Mater. Chem. A* **2018**, *6*, 16177.

[10] a) F. Garbassi, J. C. J. Bart, G. Petrini, *J. Electron Spectrosc. Relat. Phenom.* **1981**, *22*, 95; b) G. Silversmit, D. Depla, H. Poelman, G. B. Marin, R. De Gryse, *J. Electron Spectrosc. Relat. Phenom.* **2004**, *135*, 167.

[11] H. E. Kissinger, *Anal. Chem.* **1957**, *29*, 1702.

[12] C. S. Zhou, Z. G. Z. Fang, J. Lu, X. Y. Zhang, *J. Am. Chem. Soc.* **2013**, *135*, 10982.

[13] E. Grigorova, M. Khristov, P. Peshev, D. Nihtianova, N. Veliehkova, G. Atanasova, *Bulg. Chem. Commun.* **2013**, *45*, 280.

[14] K. K. Wang, X. D. Kang, Q. Kang, Y. J. Zhong, C. H. Hu, P. Wang, *J. Mater. Chem. A* **2014**, *2*, 2146.